Title

Dipole modeling of multispectral signal for detecting metallic biopsy markers during MRI-guided breast biopsy: a pilot study.

Journal

Magnetic Resonance in Medicine, 83(4)

Authors

Eskreis-Winkler, Sarah
Simon, Katherine
Reichman, Melissa
et al.

Publication Date

2020-04-01

DOI

10.1002/mrm.28017

Peer reviewed

HHS Public Access

Author manuscript

Magn Reson Med. Author manuscript; available in PMC 2021 April 01.

Published in final edited form as:

Magn Reson Med. 2020 April ; 83(4): 1380–1389. doi:10.1002/mrm.28017.

Dipole modeling of multispectral signal for detecting metallic biopsy markers during MRI-guided breast biopsy: a pilot study

Sarah Eskreis-Winkler, MD, PhD[1,2], **Katherine Simon, MD**[1], **Melissa Reichman, MD**[1], **Pascal Spincemaille, PhD**[1], **Thanh Nguyen, PhD**[1], **Youngwook Kee, PhD**[1], **Junghun Cho, MS**[1], **Paul J. Christos, DrPH**[3], **Michele Drotman, MD**[1], **Martin R. Prince, MD, PhD**[1], **Elizabeth A. Morris, MD**[2], **Yi Wang, PhD**[1]

[1]Department of Radiology, Weill Cornell Medicine, 515 E 71st Street, Suite 104, New York, NY 10021.

[2]Department of Radiology, Memorial Sloan-Kettering Cancer Center, New York, NY

[3]Division of Biostatistics and Epidemiology, Department of Healthcare Policy & Research, Weill Cornell Medicine, New York, NY

Abstract

Purpose: During MRI-guided breast biopsy, a metallic biopsy marker is deployed at the biopsy site to guide future interventions. Conventional MRI during biopsy cannot distinguish such markers from biopsy site air, and a post-biopsy mammogram is therefore performed to localize marker placement. The purpose of this pilot study is to develop dipole modeling of multispectral signal (DIMMS) as an MRI alternative to eliminate the cost, inefficiency, inconvenience and ionizing radiation of a mammogram for biopsy marker localization.

Methods: DIMMS detects and localizes the biopsy marker by fitting the measured multispectral imaging (MSI) signal to the MRI signal model and marker properties. MSI was performed on phantoms containing titanium biopsy markers and air to illustrate the clinical challenge that DIMMS addresses, and on 20 patients undergoing MRI-guided breast biopsy to assess DIMMS feasibility for marker detection. DIMMS was compared to conventional MSI field map thresholding, using the post-procedure mammogram as the reference standard.

Results: Biopsy markers were detected and localized in 20 of 20 cases using MSI with automated DIMMS post-processing (using a threshold of 0.7) and in 18 of 20 cases using MSI field mapping (using a threshold of 0.65 kHz).

Conclusion: MSI with DIMMS post-processing is a feasible technique for biopsy marker detection and localization during MRI-guided breast biopsy. With a 2-minute MSI scan, DIMMS is a promising MRI alternative to the standard-of-care post-biopsy mammogram.

Keywords

MRI-guided breast biopsy; Biopsy marker; Multispectral imaging; Quantitative modelling; Metal detection; Breast MRI

CORRESPONDING AUTHOR INFORMATION: Sarah Eskreis-Winkler, MD, PhD, Department of Radiology, Memorial Sloan Kettering Cancer Center, 300 East 66th Street, New York, NY 10065, Telephone: 646-888-5465, eskreiss@mskcc.org.

Introduction

MRI-guided breast biopsy is performed when suspicious breast lesions are detected with MRI but not seen on mammogram or ultrasound(1). During biopsy, tissue samples are obtained under MRI guidance, and a small metallic biopsy marker is deployed into the biopsy cavity to guide future interventions(2). However, conventional MRI is unable to distinguish titanium biopsy markers from the surrounding air often introduced into the breast during biopsy. Titanium and air both have high magnetic susceptibility ($\chi_{titanium} = 180 ppm$; $\chi_{air} = 9 ppm$) and appear as signal voids due to dephasing(3). Consequently, to confirm successful deployment and proper positioning of metallic biopsy markers, it is standard-of-care to obtain a post-biopsy mammogram.

Replacing the post-biopsy mammogram with a short MRI protocol would be clinically advantageous. First, it would allow women who just underwent an invasive procedure to avoid a second examination requiring “gentle”-but-still-painful compression of the just-biopsied breast. Second, it would improve workflow since patients are already in the MRI scanner (a mammogram would take longer). Third, MRI-based confirmation of marker deployment would permit immediate insertion of a second marker if the first failed to deploy (4, 5).

To confirm biopsy marker placement and to distinguish markers from surrounding air, multispectral imaging (MSI) techniques (e.g. SEMAC, MAVRIC), commonly-used for metal artifact reduction(6–15), can be retooled to selectively excite the magnetic field isocontours of metallic markers(16). There are well-established methods of computing field maps from MSI, but they are generally performed with large numbers of spectral bins(13, 17). In this work, we utilize MSI with a limited number of spectral bins as the input for a Bayesian post-processing method, which incorporates the known geometry and magnetic susceptibility of biopsy markers(6, 7) into a model for marker detection and localization. It is based on the Bayesian approach in QSM for determining object susceptibility from blooming artifacts (18–20). Our approach extends from a single magnetic dipole used in a prior work on passive tracking (21, 22) to a dipole distribution for realistic marker geometry. Of note, this work represents the first clinical application of identifying breast biopsy markers using MRI(21–24). We expect this biophysical modeling approach to be useful in cases where biopsy markers are adjacent to or partially obscured by air (25). Herein, simulations and phantom studies are presented along with validation of the proposed method in twenty patients undergoing MRI-guided breast biopsy.

METHODS

Dipole Modeling of Multispectral Signal

To determine whether or not a biopsy marker was present and, if present, to identify its spatial location, the following steps were performed: (1) The field map near the biopsy marker was modeled using the marker’s known geometry and magnetic susceptibility. (2) MRI signal was simulated for a sagittal slice with an A/P readout direction and a 125kHz readout bandwidth. (3) 3D spin echo was simulated with two RF frequencies (+0.7 kHz/+1.5

kHz). Of note, the RF excitation bandwidth was large so that there was considerable spatial overlap in the excitation profiles of the +0.7kHz and +1.5 kHz spectral bins. (4) For each slice, the spectral bin whose RF frequency offset was closest to 1.0 kHz was selected as the DIMMS input. For a given slice, the RF frequency offset refers to the difference between the frequency of the applied RF pulse and the frequency with which the spins were precessing in that slice *at the time during which the RF pulse was played out*. The precessional frequency of the spins was determined by G_{ss} the slice-selection gradient. (5) Signal normalization was performed by scaling the modeled data by the mean signal value of the acquired data for each case. (6) For a Gaussian RF excitation with frequency offset $\Delta\omega(b)$ for a given excitation b, the 3D fast spin echo k-space signal was modeled as:

$$S(t) = [\int \rho(\vec{r}) \sin(\frac{\pi}{2} e^{\frac{-\left(f(\vec{r}) + \gamma G_{ss} z - \Delta\omega(b)\right)^2}{2\sigma^2}}) e^{-i2\pi\gamma \int_0^t \left[G_x(s)x + f(\vec{r})\right] ds} e^{-i2\pi(k_y y + k_z z)} dx dy dz]$$

where $f(\vec{r})$ is the field induced by the marker, $\rho(x, y, z)$ accounts for proton density and relaxation effects, and γ is the gyromagnetic ratio/2π. (7) The cost was calculated for different marker positions and geometries in a neighborhood M around the marker:

$$E(\vec{r}_m, g) = \sum_{\vec{r}} |M(t(\vec{r}) - s(\vec{r}, \vec{r}_m, g))|^2 = \left\| M(t - s(, \vec{r}_m, g)) \right\|_2^2 \quad [1]$$

where $s(\vec{r}, \vec{r}_m, g)$ is the signal model, $t(\vec{r})$ is the measured MRI signal, g is the marker geometry and r_m is the marker location(26–28). K-means clustering identified a neighborhood M, consisting of low signal areas in the acquired data, which served as the marker search space. RF detection coil sensitivity was assumed to be approximately uniform in the region of the marker. (8) The cost function was normalized by the mean cost over all possible marker locations N:

$$E_n(g) = (N / \sum_{\vec{r}_m} |E(\vec{r}_m, g)| \cdot min_{\vec{r}_m} E(\vec{r}_m, g) \quad [2]$$

For each geometry, the location $\vec{r}_m$ corresponding to the minimum normalized energy cost was taken as the maximum likelihood location of the biopsy marker. (9) A threshold was applied, such that values of E_n below the threshold indicated that the measured and simulated MRI signal were similar enough to confirm presence of a biopsy marker, while values above the threshold indicated that the measured and simulated MRI signal were different enough to confirm absence of a marker. The marker localization method described by Eqs.1–2 is referred to as dipole modeling of multispectral signal (DIMMS).

Numerical Simulations

Numerical simulations were performed to evaluate DIMMS sensitivity to marker magnetic susceptibility, marker size, marker orientation with respect to B0, marker spatial location, the size of the region-of-interest (ROI) over which the cost metric was calculated, and the signal-to-noise ratio (SNR).

Proton density maps, magnetic susceptibility maps, and resulting field maps of rod-shaped and hourglass-shaped biopsy markers were generated in MATLAB according to the

manufacturer's specifications (Trimark, Hologic, Marlborough, MA), with the marker at the center of the image and oriented with $\varphi = \theta = 0°$ These maps were used to simulate MSI, according to the DIMMS algorithm described above.

The measured MSI signal was simulated for marker magnetic susceptibilities ranging from 100ppm-260ppm ($\chi_{true} = 180\ ppm$), for marker lengths ranging from 1mm-5mm ($length_{true} = 3mm$), for marker orientations as combinations of: $\varphi = 0°,45°,90°,135°$ and $\theta = 0°,45°,90°,135°$ and for SNRs ranging from 1.5 to 150. The ROI size over which the cost metric was calculated was varied from 3–19 voxels. A heat map was generated to illustrate the sensitivity of DIMMS to marker spatial location. For all simulations (except SNR), Gaussian noise was added to complex MRI data to achieve an SNR of 20 so as to match the noise levels in subsequent experiments.

Marker Geometry Discrimination.—Numerical simulations were performed to evaluate whether DIMMS could distinguish between rod and hourglass marker geometries at clinically-feasible spatial resolution (0.8×0.8×2.0mm). As a control, simulations were performed at unrealistically-high spatial resolution (0.1×0.1×0.1mm). At each resolution, MRI signal generated by rod and hourglass geometries were simulated without noise to generate $s(\vec{r}, \vec{r}_m, g)$ and with Gaussian noise (repeating 10 times) to generate $t(\vec{r})$. Eq. 1 was used to calculate E_{same}, the energy cost where $s(\vec{r}, \vec{r}_m, g)$ and $t(\vec{r})$ were generated using the same marker geometry, and $E_{different}$, the energy cost where $s(\vec{r}, \vec{r}_m, g)$ and $t(\vec{r})$ were generated using different marker geometries. A two-sided Student's t-test was then used to evaluate whether the difference between E_{same} and $E_{different}$ was statistically significant. These calculations were performed at clinically feasible spatial resolution and at ultra-high spatial resolution.

Phantom study

To illustrate the MRI signal patterns when a marker was separate from air versus when a marker was within an air cavity, three agarose gel-based phantoms were created. The first phantom contained a rod-shaped marker, the second contained an air cavity, and the third contained a rod-shaped marker within an air cavity.

Imaging was performed using a 1.5-T scanner (GE Medical Systems, Milwaukee, WI) with an 8-channel breast biopsy coil (Sentinelle, Invivo, Gainesville, FL). A reduced-bin 3D-MSI spin echo technique, adopted from MAVRIC, was employed with Gaussian RF pulses applied at four empirically-selected frequency offsets: −1.0, −0.2, +0.7 and +1.5 kHz. No view-angle-tilting was used. A single sagittal slab, centered at the expected location of the marker, was prescribed (TR/TE=850/17ms;slice thickness=2mm;slice number/encoded sections=8;FOV=21cm;matrix size=256×256;bandwidth=125kHz;ETL=16;sagittal acquisition;Gaussian RF excitation/refocusing pulse bandwidth=5435/2250Hz). A 3.1 mT/m selection gradient was applied during excitation to limit the spatial extent of the off-resonance excitation.

Using the DIMMS algorithm, phantoms were analyzed for the presence of a biopsy marker.

Patient study

This prospective study was approved by our Institutional Review Board and was compliant with Health Insurance Portability and Accountability Act. Informed consent was obtained from all subjects.

Patient population—Twenty women scheduled for MRI-guided breast biopsy between December 2017-June 2018 enrolled in this study.

Study Design.—Following MRI-guided breast tissue sampling, patients underwent marker deployment and reduced-bin MSI, although the order of these steps varied. For the first 10 patients (Group 1), markers were inserted before MSI. For the last 10 patients (Group 2), marker deployment failure was simulated by performing MSI prior to marker insertion. One patient in Group 2 agreed to MSI both before and after biopsy marker deployment. Titanium rod- and hourglass-shaped biopsy markers were used in all patients. All patients received a same-day post-biopsy mammogram.

MRI Protocol.—All patients were imaged with MSI. The number of slices/encoded sections varied from 8 to 14, depending on the biopsy cavity size. The MRI parameters were otherwise identical to the phantom experiment. Although four bins were acquired, only +0.7kHz and +1.5kHz were used in DIMMS. Scan time was 5.2 minutes for 4-spectral bins and 2.6 minutes for 2-spectral bins.

DIMMS Algorithm.—For each case, DIMMS determined whether or not a marker was present and, if present, identified its spatial location. For each patient, DIMMS was run twice: once assuming a rod-shaped marker and once assuming an hourglass-shaped marker.

For each Group 1 case, a radiologist evaluated MRI and mammogram to determine whether the marker deployed within an air cavity, adjacent to an air cavity, or if no air cavity was present. Air was determined by the presence of a signal void.

3D-MSI Field Map Thresholding.—To compare DIMMS to MSI field map thresholding, field maps were generated for each patient using a dictionary-matching approach(17) and deblurring technique(13). Field maps were thresholded using frequencies ranging from 200Hz to 2kHz. For each threshold, the center of mass of the thresholded voxels was taken as the biopsy marker location.

Statistical Analysis.—The study reference standard was the Group 1/Group 2 designations, denoting presence/absence of biopsy markers at the time of MSI, in combination with mammogram, which confirmed successful marker deployment for all Group 1 patients.

DIMMS and MSI field map thresholding were evaluated using E_n cut-offs between 0 and 1, and using frequency cut-offs between 200–2,000 Hz respectively. The optimal E_n cut-off for DIMMS and the optimal frequency cut-off for MSI field mapping were then used to calculate how many cases were correctly classified using each method.

All analyses were performed in SPSS Version 24.0 (IBM SPSS Statistics for Windows, Version 24.0,Armonk,NY:IBM Corp.).

RESULTS:

Numerical simulations.

Figure 1 shows DIMMS sensitivity to marker magnetic susceptibility, marker size, marker orientation, signal-to-noise ratio (SNR), and marker spatial location. As expected, E_n was minimized when the the true marker magnetic susceptibility, size, orientation, and spatial location were used. Of note, simulations demonstrate that DIMMS works irrespective of marker orientation since across all orientations, E_n remained below 0.7, the threshold established in the patient experiments. E_n decreased as SNR increased. The ROI size over which E_n was calculated did not have a measurable effect (Figure 1D).

Marker Geometry Discrimination.—DIMMS discriminated rod- and hourglass-shaped geometries at ultra-high resolution, but not at clinically-feasible spatial resolution(Figure 1F). At ultra-high spatial resolution, E_{same} was smaller than $E_{different}$ ($p<<0.001$;mean E_{same}, 0.000069;mean $E_{different}$, 0.00084). At clinically-feasible spatial resolution (i.e. the resolution of subsequent experiments), no statistically significant difference was found between E_{same} and $E_{different}$ ($p = 0.36$;mean E_{same}, 0.0074;mean $E_{different}$, 0.0074).

Phantom study

When a biopsy marker is present without surrounding air, MSI demonstrates two bright signal spots adjacent to the marker along the B0 direction(Figure 2A–C). When a biopsy marker rests within air, one of the bright spots is obscured(Figure 2G–I). DIMMS results for the biopsy marker, air cavity, and biopsy marker partially obscured by air cavity were: 0.51, 0.86 and 0.67. Applying a 0.7 threshold, DIMMS correctly indicated that a biopsy marker was present in the first and third cases, but not in the second.

Patient study

MSI, MSI field mapping, and post-biopsy mammograms were successfully performed on all patients(see Figure 3). In cases with a biopsy marker present, 30% of markers deployed within an air cavity, 30% adjacent to an air cavity, and 40% without air present.

At an E_n cut-off of 0.70, DIMMS correctly detected and localized the biopsy markers in 20 of 20 cases. For all cases, irrespective of marker geometry, DIMMS identified the same biopsy marker location(see Figure 4).

For MSI field maps containing both biopsy marker and air, the marker-induced field was higher than the air-induced field, but it was not possible to set a global field threshold that worked across cases. The air-induced field for some cases was higher than the marker-induced field for other cases(see Figure 3). Thresholding performed best with a 0.65kHz cut-off, when it correctly detected and localized the markers in 18 of 20 cases.

DISCUSSION

Our results demonstrate DIMMS feasibility for metallic biopsy marker detection during MRI-guided breast biopsy. DIMMS biophysical modeling distinguishes MRI signal patterns induced by biopsy markers from those induced by air and tissue. We used DIMMS to identify titanium biomarkers at 1.5T. Further studies will be needed to show performance for other metallic biopsy markers and at higher field strengths.

DIMMS works because it incorporates prior information about biopsy marker geometry and physical composition in both the data acquisition and data post-processing steps. This Bayesian approach has been very effective for QSM in accurately measuring iron in oxygen consumption(29), deep gray nuclei for neurostimulation(30), multiple sclerosis(31–33), cerebral cavernous malformations(34), Alzheimer's disease(35–37), Parkinson's disease(38), and Huntington's disease(39). The iron susceptibility values in these diseases are less than 3ppm, and there is ample phase information for iron mapping. In contrast, for metallic markers with susceptibility values greater than 100ppm, strong field inhomogeneities make it difficult to map the neighboring field. The MSI acquisition, tailored to capture the field spectrum induced by titanium biopsy markers, can improve data acquisition over gradient echo (17). The post-processing algorithm in DIMMS incorporates the biopsy marker's biophysical properties into a piece-wise constant model, thus vastly reducing the number of unknowns and correspondingly reducing scan time for input data to an acceptable two minutes(40).

In this pilot study, DIMMS achieved better marker detection than MSI field map thresholding. MSI field mapping does not directly reflect local tissue magnetic properties but is instead a weighted summation from all surrounding magnetic susceptibility sources. Specifically, the field depends on the surrounding air geometry, making it difficult to establish a global field threshold. In contrast, DIMMS biophysically models the metallic marker-induced MRI signal for establishing an intrinsic marker property, characterized here by a normalized energy cost. DIMMS achieved promising results in this pilot study, although further validation in a larger patient population is warranted. Particularly, it will be important to evaluate DIMMS in challenging cases, such as when the marker lands within an air cavity which partially obscures the marker-induced MRI signal.

This initial feasibility study had several limitations. To minimize workflow disruptions, MSI was acquired *before* the breast was released from compression by the biopsy coil. Marker migration may occur as the breast is released from compression ("accordion effect") (41–43). Future studies should perform MSI while the patient is prone on the MRI table, but *after* the breast is released from compression. This modification could capture the final resting place of the biopsy marker and create a clinically-viable alternative to the post-biopsy mammogram. Here we ran DIMMS on sagittal slices, but this work may be extended to 3D in the future. DIMMS, which was shown to be promising here using simply +0.7kHz and +1.5 kHz spectral bins, could also be further improved with careful optimization of the spectral bin frequency choices. Our MSI acquisition used a high receiver bandwidth to simplify marker localization by decreasing readout shift artifact. However, MSI with low receiver bandwidth has the potential to increase DIMMS sensitivity to the presence of metal,

and we plan to investigate this promising alternative in future work. Additionally, given the variable distribution of fat in the breast, water and fat maps may be incorporated into the model to improve robustness. Scan time may also be further shortened with 2D MSI(11). Finally, high resolution imaging should be further investigated to differentiate rod versus hourglass geometries, which would be helpful in patients with multiple markers from multiple biopsies. Our numerical simulations suggest that both higher SNR and less partial volume averaging will improve performance; further work is needed to determine the relative contributions of these factors.

In conclusion, DIMMS is a clinically-feasible technique for biopsy marker detection during MRI-guided biopsy, eliminating the cost, inefficiency, inconvenience and ionizing radiation of standard-of-care post-biopsy mammogram. This new quantitative breast imaging application warrants further validation with a larger sample size for clinical translation. Although this work focuses on DIMMS as a tool for breast biopsy marker detection, it might be used in any MRI-guided procedure requiring tracking of other metallic markers including radioactive seeds, electrodes, or other paramagnetic devices.

ACKNOWLEDGEMENTS

Grant support: S10 OD021782, Clinical and Translational Science Center at Weill Cornell Medical College (1-UL1-TR002384–01).

REFERENCES

1. Morris EA. Diagnostic breast MR imaging: current status and future directions. Magn Reson Imaging Clin N Am. 2010;18(1):57–74. Epub 2009/12/08. doi: 10.1016/j.mric.2009.09.005. [PubMed: 19962093]
2. Mahoney MC, Newell MS. Breast Intervention: How I Do It. Radiology. 2013;268(1):12–24. doi: 10.1148/radiol.13120985. [PubMed: 23793589]
3. Schenck JF. The role of magnetic susceptibility in magnetic resonance imaging: MRI magnetic compatibility of the first and second kinds. Medical Physics. 1996;23(6):815–50. doi: Doi 10.1118/1.597854. [PubMed: 8798169]
4. Bourke AG, Peter P, Jose CL. The disappearing clip: an unusual complication in MRI biopsy. BMJ Case Rep. 2014;2014 Epub 2014/08/21. doi: 10.1136/bcr-2014-204092.
5. Esserman LE, Cura MA, DaCosta D. Recognizing pitfalls in early and late migration of clip markers after imaging-guided directional vacuum-assisted biopsy. Radiographics: a review publication of the Radiological Society of North America, Inc. 2004;24(1):147–56. Epub 2004/01/20. doi: 10.1148/rg.241035052.
6. Genson CC, Blane CE, Helvie MA, Waits SA, Chenevert TL. Effects on breast MRI of artifacts caused by metallic tissue marker clips. AJR American journal of roentgenology. 2007;188(2):372–6. Epub 2007/01/24. doi: 10.2214/AJR.05.1254. [PubMed: 17242244]
7. Shellock FG. Metallic marking clips used after stereotactic breast biopsy: Ex vivo testing of ferromagnetism, heating, and artifacts associated with MR imaging. American Journal of Roentgenology. 1999;172(5):1417–9. doi: DOI 10.2214/ajr.172.5.10227529. [PubMed: 10227529]
8. Hargreaves BA, Worters PW, Pauly KB, Pauly JM, Koch KM, Gold GE. Metal-Induced Artifacts in MRI. American Journal of Roentgenology. 2011;197(3):547–55. doi: 10.2214/Ajr.11.7364. [PubMed: 21862795]
9. Lu WM, Pauly KB, Gold GE, Pauly JM, Hargreaves BA. SEMAC: Slice Encoding for Metal Artifact Correction in MRI. Magn Reson Med. 2009;62(1):66–76. doi: 10.1002/mrm.21967. [PubMed: 19267347]

10. Koch KM, Lorbiecki JE, Hinks RS, King KF. A Multispectral Three-Dimensional Acquisition Technique for Imaging Near Metal Implants. Magnetic Resonance in Medicine. 2009;61(2):381–90. doi: 10.1002/mrm.21856. [PubMed: 19165901]
11. Hargreaves BA, Taviani V, Litwiller DV, Yoon D. 2D multi-spectral imaging for fast MRI near metal. Magnetic Resonance in Medicine. 2018;79(2):968–73. doi: 10.1002/mrm.26724. [PubMed: 28444805]
12. Koch KM, Brau AC, Chen W, Gold GE, Hargreaves BA, Koff M, et al. Imaging Near Metal with a MAVRIC-SEMAC Hybrid. Magn Reson Med. 2011;65(1):71–82. doi: 10.1002/mrm.22523. [PubMed: 20981709]
13. Quist B, Shi XW, Weber H, Hargreaves BA. Improved Field-Mapping and Artifact Correction in Multispectral Imaging. Magn Reson Med. 2017;78(5):2022–34. doi: 10.1002/mrm.26597. [PubMed: 28261847]
14. Hargreaves BA, Chen WT, Lu WM, Alley MT, Gold GE, Brau ACS, et al. Accelerated Slice Encoding for Metal Artifact Correction. Journal of Magnetic Resonance Imaging. 2010;31(4):987–96. doi: 10.1002/jmri.22112. [PubMed: 20373445]
15. Hargreaves BA, Daniel BL. Metals in MR-mammography: how to deal with it? Eur J Radiol. 2012;81 Suppl 1:S56–8. doi: 10.1016/S0720-048X(12)70021-9. [PubMed: 23083602]
16. Eskreis-Winkler Sea, editor Feasibility of multispectral spin echo breast QSM: an alternative to post-biopsy mammogram after MRI-guided breast biopsy. ISMRM; 2018.
17. Shi XW, Yoon D, Koch KM, Hargreaves BA. Metallic Implant Geometry and Susceptibility Estimation Using Multispectral B-0 Field Maps. Magn Reson Med. 2017;77(6):2402–13. doi: 10.1002/mrm.26313. [PubMed: 27385493]
18. Wang Y, Liu T. Quantitative Susceptibility Mapping (QSM): Decoding MRI Data for a Tissue Magnetic Biomarker. Magnetic Resonance in Medicine. 2015;73(1):82–101. doi: 10.1002/mrm.25358. [PubMed: 25044035]
19. Li J, Chang S, Liu T, Wang Q, Cui D, Chen X, et al. Reducing the object orientation dependence of susceptibility effects in gradient echo MRI through quantitative susceptibility mapping. Magnetic resonance in medicine: official journal of the Society of Magnetic Resonance in Medicine / Society of Magnetic Resonance in Medicine. 2012;68(5):1563–9. doi: 10.1002/mrm.24135.
20. de Rochefort L, Liu T, Kressler B, Liu J, Spincemaille P, Lebon V, et al. Quantitative Susceptibility Map Reconstruction from MR Phase Data Using Bayesian Regularization: Validation and Application to Brain Imaging. Magnetic Resonance in Medicine. 2010;63(1):194–206. doi: 10.1002/mrm.22187. [PubMed: 19953507]
21. Seppenwoolde JH, Viergever MA, Bakker CJ. Passive tracking exploiting local signal conservation: the white marker phenomenon. Magnetic resonance in medicine: official journal of the Society of Magnetic Resonance in Medicine / Society of Magnetic Resonance in Medicine. 2003;50(4):784–90.
22. Felfoul O, Mathieu JB, Beaudoin G, Martel S. In vivo MR-tracking based on magnetic signature selective excitation. IEEE Trans Med Imaging. 2008;27(1):28–35. Epub 2008/02/14. doi: 10.1109/TMI.2007.897375. [PubMed: 18270059]
23. Stuber M, Gilson WD, Schar M, Kedziorek DA, Hofmann LV, Shah S, et al. Positive contrast visualization of iron oxide-labeled stem cells using inversion-recovery with ON-resonant water suppression (IRON). Magnetic resonance in medicine: official journal of the Society of Magnetic Resonance in Medicine / Society of Magnetic Resonance in Medicine. 2007;58(5):1072–7. Epub 2007/10/31. doi: 10.1002/mrm.21399.
24. Zhang K, Maier F, Krafft AJ, Umathum R, Semmler W, Bock M. Tracking of an interventional catheter with a ferromagnetic tip using dual-echo projections. J Magn Reson. 2013;234:176–83. Epub 2013/07/31. doi: 10.1016/j.jmr.2013.06.020. [PubMed: 23892103]
25. Eskreis-Winkler Sea, editor Oligospectral MRI (oMRI): A New Technique for Metallic Biopsy Marker Detection During MRI-Guided Breast Biopsy. Breast MRI ISMRM Workshop; 2018; Las Vegas, NV.
26. Jackson J. Classical Electrodynamics. 3rd ed New York: Wiley; 1999.
27. Haacke EM BR, Thompson MR. Magnetic Resonance Imaging: Physical Principles and Sequence Design. New York: Wiley-Liss; 1999.

28. Wang Y. Principles of Magnetic Resonance Imaging: physics concepts, pulse sequences and biomedical applications. Ithaca, NY 2014.
29. Deh K, Nguyen TD, Eskreis-Winkler S, Prince MR, Spincemaille P, Gauthier S, et al. Reproducibility of quantitative susceptibility mapping in the brain at two field strengths from two vendors. J Magn Reson Imaging. 2015;42(6):1592–600. Epub 2015/05/12. doi: 10.1002/jmri.24943. [PubMed: 25960320]
30. Dimov A, Patel W, Yao Y, Wang Y, O'Halloran R, Kopell BH. Iron concentration linked to structural connectivity in the subthalamic nucleus: implications for deep brain stimulation. J Neurosurg. 2019:1–8. doi: 10.3171/2018.8.JNS18531.
31. Chen W, Gauthier SA, Gupta A, Comunale J, Liu T, Wang S, et al. Quantitative Susceptibility Mapping of Multiple Sclerosis Lesions at Various Ages. Radiology. 2014;271(1):183–92. doi: 10.1148/radiol.13130353. [PubMed: 24475808]
32. Zhang Y, Gauthier SA, Gupta A, Tu L, Comunale J, Chiang GC, et al. Magnetic Susceptibility from Quantitative Susceptibility Mapping Can Differentiate New Enhancing from Nonenhancing Multiple Sclerosis Lesions without Gadolinium Injection. AJNR Am J Neuroradiol. 2016;37(10):1794–9. Epub 2016/07/02. doi: 10.3174/ajnr.A4856. [PubMed: 27365331]
33. Wisnieff C, Ramanan S, Olesik J, Gauthier S, Wang Y, Pitt D. Quantitative susceptibility mapping (QSM) of white matter multiple sclerosis lesions: Interpreting positive susceptibility and the presence of iron. Magnetic resonance in medicine: official journal of the Society of Magnetic Resonance in Medicine / Society of Magnetic Resonance in Medicine. 2015;74(2):564–70. doi: 10.1002/mrm.25420.
34. Tan H, Liu T, Wu Y, Thacker J, Shenkar R, Mikati AG, et al. Evaluation of iron content in human cerebral cavernous malformation using quantitative susceptibility mapping. Invest Radiol. 2014;49(7):498–504. doi: 10.1097/RLI.0000000000000043. [PubMed: 24619210]
35. Acosta-Cabronero J, Williams GB, Cardenas-Blanco A, Arnold RJ, Lupson V, Nestor PJ. In vivo quantitative susceptibility mapping (QSM) in Alzheimer's disease. PLoS One. 2013;8(11):e81093. doi: 10.1371/journal.pone.0081093. [PubMed: 24278382]
36. Ayton S, Fazlollahi A, Bourgeat P, Raniga P, Ng A, Lim YY, et al. Cerebral quantitative susceptibility mapping predicts amyloid-beta-related cognitive decline. Brain. 2017;140(8):2112–9. Epub 2017/09/14. doi: 10.1093/brain/awx137. [PubMed: 28899019]
37. Kim HG, Park S, Rhee HY, Lee KM, Ryu CW, Rhee SJ, et al. Quantitative susceptibility mapping to evaluate the early stage of Alzheimer's disease. Neuroimage Clin. 2017;16:429–38. Epub 2017/09/08. doi: 10.1016/j.nicl.2017.08.019. [PubMed: 28879084]
38. Murakami Y, Kakeda S, Watanabe K, Ueda I, Ogasawara A, Moriya J, et al. Usefulness of quantitative susceptibility mapping for the diagnosis of Parkinson disease. AJNR Am J Neuroradiol. 2015;36(6):1102–8. Epub 2015/03/15. doi: 10.3174/ajnr.A4260. [PubMed: 25767187]
39. van Bergen JM, Hua J, Unschuld PG, Lim IA, Jones CK, Margolis RL, et al. Quantitative Susceptibility Mapping Suggests Altered Brain Iron in Premanifest Huntington Disease. AJNR Am J Neuroradiol. 2016;37(5):789–96. Epub 2015/12/19. doi: 10.3174/ajnr.A4617. [PubMed: 26680466]
40. de Rochefort L, Brown R, Prince MR, Wang Y. Quantitative MR susceptibility mapping using piece-wise constant regularized inversion of the magnetic field. Magn Reson Med. 2008;60(4):1003–9. doi: 10.1002/mrm.21710. [PubMed: 18816834]
41. Burbank F, Forcier N. Tissue marking clip for stereotactic breast biopsy: initial placement accuracy, long-term stability, and usefulness as a guide for wire localization. Radiology. 1997;205(2):407–15. Epub 1997/11/14. doi: 10.1148/radiology.205.2.9356621. [PubMed: 9356621]
42. Rosen EL, Vo TT. Metallic clip deployment during stereotactic breast biopsy: retrospective analysis. Radiology. 2001;218(2):510–6. Epub 2001/02/13. doi: 10.1148/radiology.218.2.r01fe39510. [PubMed: 11161170]
43. Liberman L, Dershaw DD, Morris EA, Abramson AF, Thornton CM, Rosen PP. Clip placement after stereotactic vacuum-assisted breast biopsy. Radiology. 1997;205(2):417–22. Epub 1997/11/14. doi: 10.1148/radiology.205.2.9356622. [PubMed: 9356622]

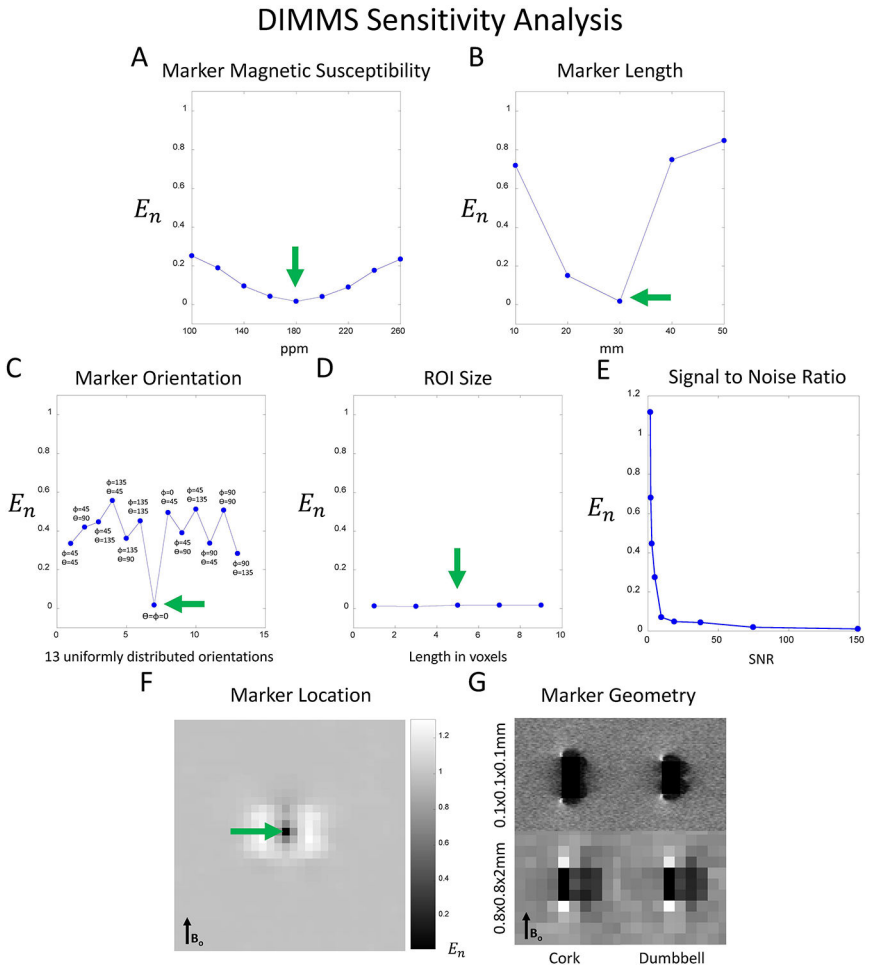

Figure 1:

DIMMS sensitivity analysis. Normalized energy cost, E_n is lowest: A) at the true marker magnetic susceptibility (χ = 180ppm), B) at the true marker length (3mm), and C) at the true marker orientation with respect to B0 (φ = 0°, θ = 0°). D) The size of the square-shaped ROI over which E_n is calculated does not have a measurable effect. E) E_n decreases as signal to noise ratio increases. F) An E_n heat map shows that the minimum cost is achieved at the true marker location. G) Numerical simulations of MRI signal, at a frequency offset of +0.7 kHz, generated by rod and hourglass-shaped biopsy markers show that discrimination of marker geometry is possible at ultra-high spatial resolution (0.1 × 0.1 × 0.1 mm), but not at clinically-achievable resolution (0.8 × 0.8 × 2.0 mm).

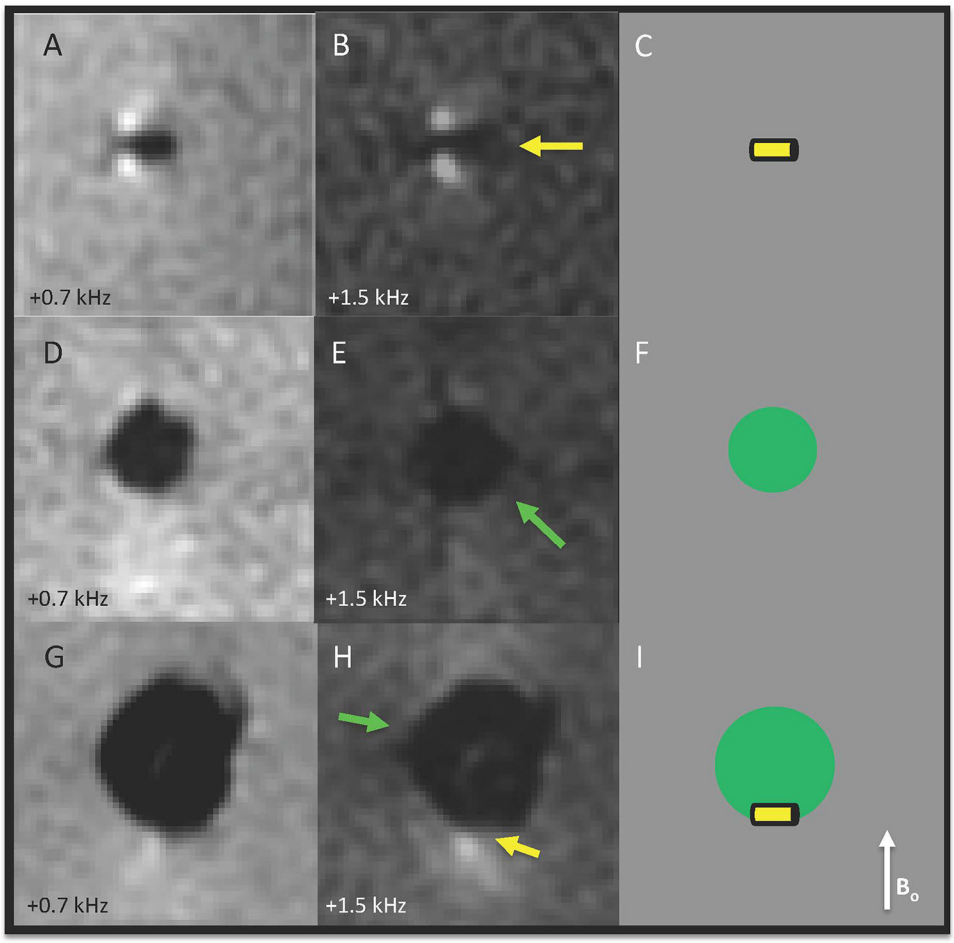

Figure 2:
Phantom illustrates that air may partially mask the marker-induced signal, creating the need for quantitative modeling to determine whether or not a biopsy marker is present. A) & B) show a rod-shaped biopsy marker (yellow arrow), with corresponding diagram in C). D) & E) show an air cavity, with corresponding diagram in F). G) & H) show a rod-shaped biopsy marker resting within an air cavity, which partially obscures the marker-induced signal, with corresponding diagram in I).

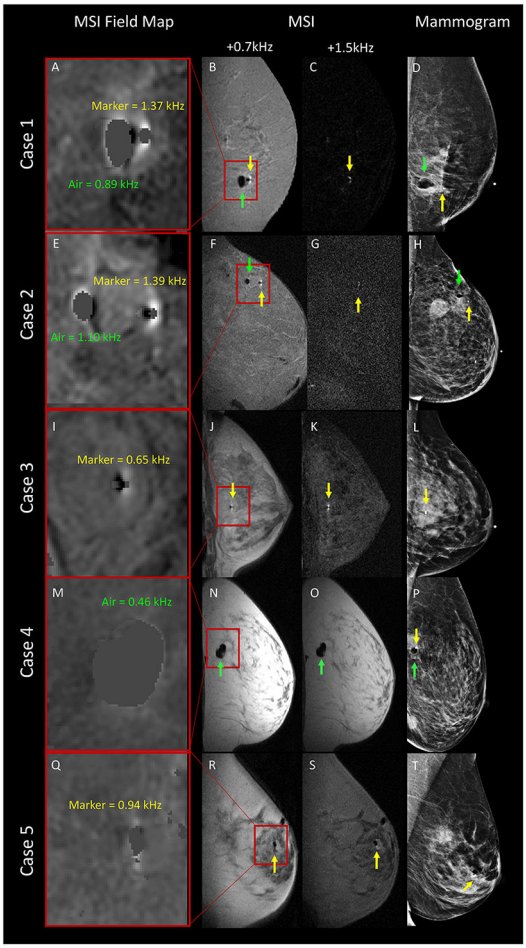

Figure 3:

Sagittal MSI field maps insets, sagittal MSI raw data, and mediolateral mammograms performed at the end of MRI-guided breast biopsy in five patients. For MSI field maps (A, E, I, M Q), maximum values of marker-induced and air-induced fields are shown in yellow and green. Cases 1 & 2: a biopsy marker (yellow arrow) and air (green arrow) are present. Case 3: biopsy marker is present (yellow arrow). Case 4: air is present (green arrow). Case 5: challenging case where biopsy marker lands within air cavity. On visual inspection of raw MSI data (R & S), it is unclear whether a biopsy marker is present, however DIMMS correctly identified the marker location within the air cavity. The maximum MSI field map value of 0.94 kHz (Q) was not helpful in confirming the presence of the marker as MSI field map values of up to 1.1 kHz can be seen with air alone (E).

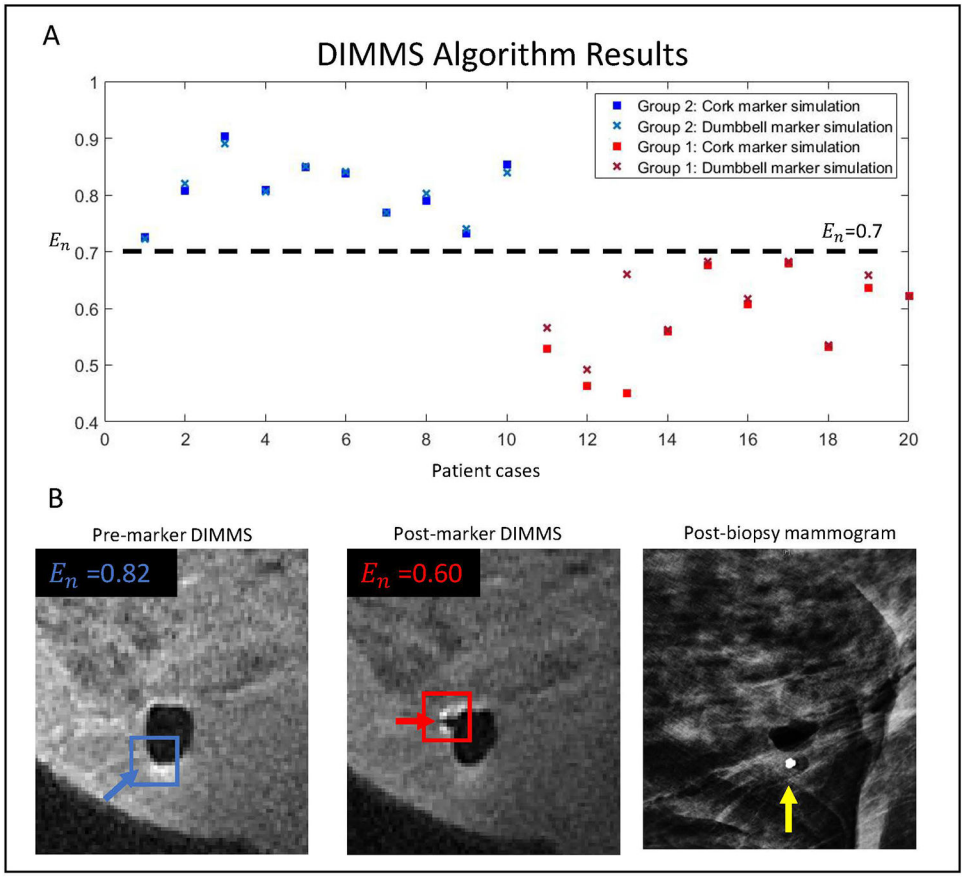

Figure 4:

DIMMS Algorithm Results. A) Normalized cost function, E_n, is plotted for each case. A threshold of 0.70 discriminates whether or not a biopsy marker is present, irrespective of biopsy marker geometry. B) 71-year old woman undergoing MRI-guided breast biopsy with DIMMS pre- and post-marker placement. Blue and red arrows show the location with the minimum cost for the pre-marker and post-marker images. As expected, pre-marker cost was greater than post-marker cost. Post-biopsy mammogram confirms biopsy marker location (yellow arrow).